

# NASICON $\text{Li}_{1.2}\text{Mg}_{0.1}\text{Zr}_{1.9}(\text{PO}_4)_3$ Solid Electrolyte for an All-Solid-State Li-Metal Battery

Qiongyu Zhou, Biyi Xu, Po-Hsiu Chien, Yutao Li,\* Bing Huang, Nan Wu, Henghui Xu, Nicholas S. Grundish, Yan-Yan Hu, and John B. Goodenough\*

A thin solid electrolyte with a high  $\text{Li}^+$  conductivity is used to separate the metallic lithium anode and the cathode in an all-solid-state Li-metal battery. However, most solid Li-ion electrolytes have a small electrochemical stability window, large interfacial resistance, and cannot block lithium-dendrite growth when lithium is plated on charging of the cell.  $\text{Mg}^{2+}$  stabilizes a rhombohedral NASICON-structured solid electrolyte of the formula  $\text{Li}_{1.2}\text{Mg}_{0.1}\text{Zr}_{1.9}(\text{PO}_4)_3$  (LMZP). This solid electrolyte has Li-ion conductivity two orders of magnitude higher at 25 °C than that of the triclinic  $\text{LiZr}_2(\text{PO}_4)_3$ .  $^7\text{Li}$  and  $^6\text{Li}$  NMR confirm the Li-ions in two different crystallographic sites of the NASICON framework with 85% of the Li-ions having a relatively higher mobility than the other 15%. The anode–electrolyte interface is further investigated with symmetric Li/LMZP/Li cell testing, while the cathode–electrolyte interface is explored with an all-solid-state Li/LMZP/LiFePO<sub>4</sub> cell. The enhanced performance of these cells enabled by the  $\text{Li}_{1.2}\text{Mg}_{0.1}\text{Zr}_{1.9}(\text{PO}_4)_3$  solid electrolyte is stable upon repeated charge/discharge cycling.

## 1. Introduction

The need to develop a safe all-solid-state Li-metal battery with performance comparable to or better than commercial rechargeable Li-ion batteries with a toxic and flammable organic liquid electrolyte has stimulated intense research efforts into  $\text{Li}^+$  solid electrolytes.<sup>[1–5]</sup> Moreover, a solid electrolyte serves as a critical component in enabling Li–S and Li–air batteries as it prevents the diffusion of dissolved species (e.g., sulfide polyanions) toward the Li-metal anode.<sup>[6–8]</sup> For these applications, the fast  $\text{Li}^+$  conducting solid electrolyte should have a large electrochemical window, fast  $\text{Li}^+$  transfer across the electrolyte/electrode interface, and an overall thickness of less than 20  $\mu\text{m}$ . Oxide-based  $\text{Li}^+$  conductors are good candidates for these batteries owing to their

stability in air and larger electrochemical windows compared to sulfide and halide electrolytes. In framework crystal structures such as LISICON ( $\text{Li}_{11-x}\text{Me}_{2-x}\text{P}_{1+x}\text{S}_{12}$  with  $\text{Me} = \text{Ge}, \text{Sn}$ ),<sup>[9,10]</sup> garnet (e.g.,  $\text{Li}_{7-x}\text{La}_3\text{Zr}_{2-x}\text{Ta}_x\text{O}_{12}$ ),<sup>[11]</sup> NASICON (e.g.,  $\text{Li}_{1+x}\text{Al}_x(\text{Ti}/\text{Ge})_{2-x}(\text{PO}_4)_3$ ),<sup>[12–15]</sup> perovskite (e.g.,  $\text{Li}_{0.33}\text{La}_{0.55}\text{TiO}_3$ ),<sup>[16]</sup> and antiperovskite electrolytes (e.g.,  $\text{Li}_{3-x}\text{OH}_x\text{Cl}$ ),<sup>[17]</sup> the  $\text{Li}^+$  sites and  $\text{Li}^+$  vacancies form a 3D and size-matched channel for  $\text{Li}^+$  movement. However, most oxide electrolytes show a large resistance at the solid-electrolyte/electrode interfaces because of the mechanically rigid physical contact intrinsic to a solid–solid interface as well as a weak chemical interaction between the solid electrolyte and the electrode. Additionally, solid electrolytes with strong  $\text{Li}^+ - \text{O}^{2-}$  ionic bonds are usually unstable in air, resulting in the formation of a surface layer largely consisting of  $\text{Li}^+$ -insulating compounds (e.g.,  $\text{Li}_2\text{CO}_3$  and  $\text{LiOH}$ ).<sup>[18,19]</sup> This surface layer has several attributes detrimental to the material's capability to serve as a viable solid electrolyte; 1)  $\text{Li}^+$  movement across grain boundaries and at the electrolyte/electrode interface is severely slowed, and 2) the wettability of the solid electrolyte by a Li-metal anode is drastically reduced, causing poor interfacial compatibility. Exploring new materials for a solid electrolyte that is stable in air with a high  $\text{Li}^+$  conductivity and a small resistance at the solid-electrolyte/electrode interface remains a great challenge in establishing a commercially viable all-solid-state battery.

Several compounds have provided hope for a competitive solid electrolyte. The NASICON-structured  $\text{Li}_{1.3}\text{Al}_{0.3}\text{Ti}_{1.7}(\text{PO}_4)_3$  shows a maximum bulk  $\text{Li}^+$  conductivity of  $10^{-3} \text{ S cm}^{-1}$  at

Dr. Q. Y. Zhou  
School of Materials Science and Energy Engineering  
Foshan University  
Foshan 528000, P. R. China


Dr. Q. Y. Zhou, Dr. B. Y. Xu, Dr. Y. Li, Dr. N. Wu, Dr. H. H. Xu,  
N. S. Grundish, Prof. J. B. Goodenough  
Materials Science and Engineering Program and Texas Materials Institute  
The University of Texas at Austin  
Austin, TX 78712, USA  
E-mail: lytthu@utexas.edu; jgoodenough@mail.utexas.edu

Dr. P.-H. Chien, Prof. Y.-Y. Hu  
Department of Chemistry and Biochemistry  
Florida State University  
Tallahassee, FL 32306, USA

Dr. P.-H. Chien, Prof. Y.-Y. Hu  
National High Magnetic Field Laboratory  
Tallahassee, FL 32310, USA

Dr. P.-H. Chien  
Neutron Scattering Division  
Oak Ridge National Laboratory  
Tallahassee, FL 37830, USA

B. Huang  
State Key Lab of New Ceramics and Fine Processing  
School of Materials Science and Engineering  
Tsinghua University  
Beijing 100084, P. R. China

 The ORCID identification number(s) for the author(s) of this article can be found under <https://doi.org/10.1002/smt.202000764>.

DOI: 10.1002/smt.202000764

25 °C and is water-stable, providing a small interfacial resistance in aqueous Li-air batteries. Unfortunately, the  $\text{Ti}^{4+}$  present in  $\text{Li}_{1.3}\text{Al}_{0.3}\text{Ti}_{1.7}(\text{PO}_4)_3$  is easily reduced at low voltages ( $<2$  V versus  $\text{Li}^+/\text{Li}$ ), making it chemically unstable against Li metal.<sup>[20–23]</sup> NASICON-structured  $\text{LiZr}_2(\text{PO}_4)_3$  provides a more electrochemically stable option than  $\text{Li}_{1.3}\text{Al}_{0.3}\text{Ti}_{1.7}(\text{PO}_4)_3$  because the energy of the  $\text{Zr}^{4+}/\text{Zr}^0$  redox couple in  $\text{LiZr}_2(\text{PO}_4)_3$  is above the Fermi level of Li metal. The crystal structure of  $\text{LiZr}_2(\text{PO}_4)_3$  is highly dependent on the sintering temperature and has four different crystalline phases. The rhombohedral  $\text{LiZr}_2(\text{PO}_4)_3$  prepared at high temperatures shows the best  $\text{Li}^+$  conductivity but is only stable at temperatures above 50 °C,<sup>[24,25]</sup> and does not show ionic conductivity to the levels required for full cell battery operation at room temperature. This lack of sufficient conductivity compared to the  $\text{Li}_{1.3}\text{Al}_{0.3}\text{Ti}_{1.7}(\text{PO}_4)_3$  material stems from the small  $\text{Li}^+$  population in  $\text{LiZr}_2(\text{PO}_4)_3$  relative to the available Li-sites in the NASICON framework. We recently reported the preparation of the rhombohedral  $\text{LiZr}_2(\text{PO}_4)_3$  phase with acetate precursor materials.<sup>[26]</sup> The resulting material showed excellent  $\text{Li}^+$  transfer across the Li/ $\text{LiZr}_2(\text{PO}_4)_3$  interface.

We have introduced  $\text{Ca}^{2+}/\text{Y}^{3+}$  doping to stabilize the rhombohedral  $\text{LiZr}_2(\text{PO}_4)_3$  phase at room temperature;<sup>[27,25]</sup> however, the Li-ion local environment and the performance of the doped  $\text{LiZr}_2(\text{PO}_4)_3$  in an all-solid-state Li-metal battery are not characterized. In this work, we set out to improve the Li-ion population in the NASICON framework starting from  $\text{LiZr}_2(\text{PO}_4)_3$  with  $\text{Mg}^{2+}$ -

doping. This doping strategy improves the  $\text{Li}^+$  conductivity of  $\text{LiZr}_2(\text{PO}_4)_3$  by increasing the  $\text{Li}^+$  concentration in the material as well as by stabilizing the rhombohedral phase of the material at 25 °C by introducing  $\text{Mg}^{2+}$  into the structure.  $^6\text{Li}$  NMR was performed to examine the local  $\text{Li}^+$  environments and the mobilities of  $\text{Li}^+$ -ions in different sites of  $\text{Li}_{1.2}\text{Mg}_{0.1}\text{Zr}_{1.9}(\text{PO}_4)_3$  (LMZP). The  $\text{Li}_{1.2}\text{Mg}_{0.1}\text{Zr}_{1.9}(\text{PO}_4)_3$  solid electrolyte was tested in symmetric Li/LMZP/Li cells and all-solid-state Li-metal batteries with an  $\text{LiFePO}_4$  cathode. Ex situ time-of-flight secondary ion mass spectrometry (TOF-SIMS) on a LMZP pellet cycled in a symmetric Li/LMZP/Li cell confirmed the chemical formation of a  $\text{Li}_3\text{P}$  layer that allows fast  $\text{Li}^+$ -transfer across the Li/LMZP interface and suppresses dendrite formation during lithium plating.

## 2. Results and Discussion

The samples of  $\text{Li}_{1+2x}\text{Mg}_x\text{Zr}_{2-x}(\text{PO}_4)_3$  ( $0.05 \leq x \leq 0.15$ ) for diffraction and ionic conductivity measurements were prepared with two different sintering methods. A set of samples for each composition of  $x = 0.05$ ,  $x = 0.1$ , and  $x = 0.15$  were sintered by conventional sintering (CS) in a box furnace, and a separate set of samples for each of the aforementioned compositions were sintered via spark plasma sintering (SPS). The X-ray diffraction (XRD) patterns of these samples are shown in Figure 1a and Figure S1 in the Supporting Information. Two

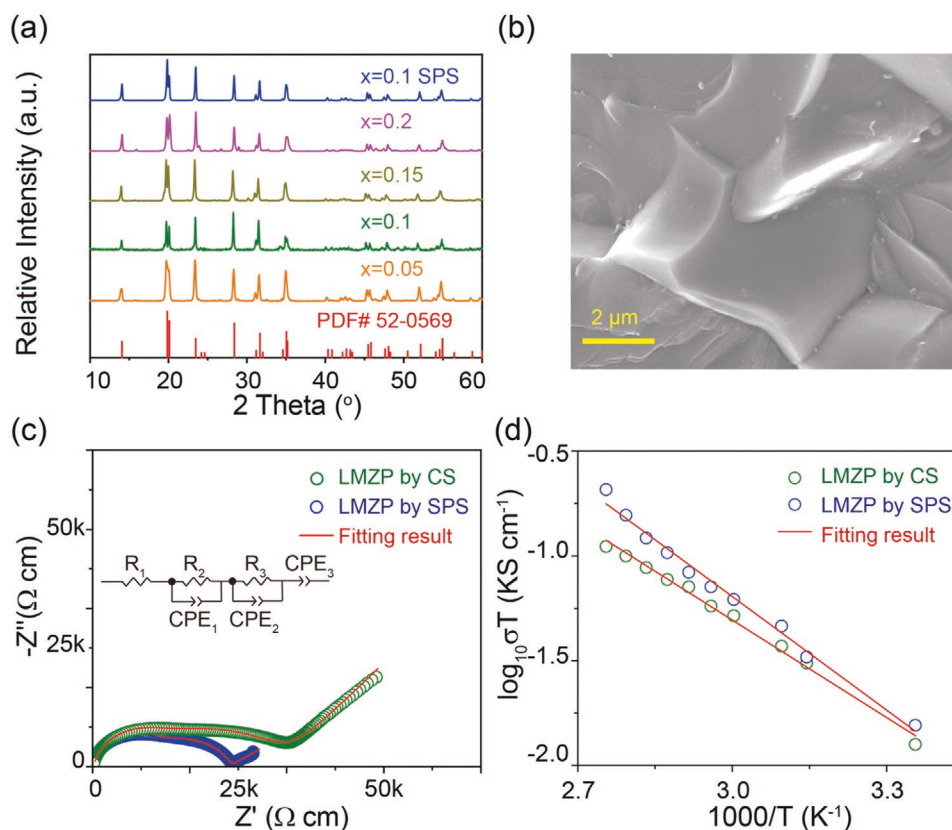


**Figure 1.** a) XRD patterns of  $\text{Li}_{1+2x}\text{Mg}_x\text{Zr}_{2-x}(\text{PO}_4)_3$  samples ( $0.05 \leq x \leq 0.15$ ) sintered by CS and SPS, b) cross-sectional SEM image of  $\text{Li}_{1.2}\text{Mg}_{0.1}\text{Zr}_{1.9}(\text{PO}_4)_3$  (LMZP) pellet sintered by SPS at 1050 °C for 10 min, c) room-temperature electrochemical impedance spectra (inset: equivalent circuit), and d) Arrhenius plots of LMZP pellet sintered by CS and SPS in the temperature range of 298–370 K.

complimentary factors dictate the phase composition of the final  $\text{Li}_{1+2x}\text{Mg}_x\text{Zr}_{2-x}(\text{PO}_4)_3$  samples at 25 °C, the sintering temperature and  $\text{Mg}^{2+}$  doping concentration. The  $\text{Li}_{1+2x}\text{Mg}_x\text{Zr}_{2-x}(\text{PO}_4)_3$  samples ( $x = 0.05, 0.1$ , and  $0.15$ ) fired at 1150 °C for 16 h by CS have a pure rhombohedral phase (space group:  $R\bar{3}c$ ); impurity phases began to show in the sample with  $x = 0.2$ . Refinement of the XRD patterns of  $\text{Li}_{1+2x}\text{Mg}_x\text{Zr}_{2-x}(\text{PO}_4)_3$  ( $x = 0.05, 0.1$ , and  $0.15$ ) showed a slight reduction of lattice parameter  $a$  and a slight increase of lattice parameter  $c$  (Figure S1c, Supporting Information) compared to those reported for the rhombohedral  $\text{LiZr}_2(\text{PO}_4)_3$  phase at 150 °C.<sup>[28]</sup> The minute change in the  $a$  and  $c$  lattice parameters in the doped samples can be attributed to  $\text{Mg}^{2+}$  and  $\text{Zr}^{4+}$  having the same ionic radius of 0.72 Å. Pure rhombohedral phase LMZP pellets were also obtained at 1050 °C for 10 min with SPS. The molar ratio of  $\text{Li}^+$ ,  $\text{Mg}^{2+}$ , and  $\text{Zr}^{4+}$  in LMZP, confirmed by ICP, was 1.28:0.11:1.86; the higher  $\text{Li}^+$  concentration is attributed to the excess lithium precursor added during preparation. The LMZP ( $x = 0.1$ ) pellet prepared by SPS has a much higher density (2.95 g cm<sup>-3</sup>) than that of the CS pellet (2.66 g cm<sup>-3</sup>), which is confirmed with scanning electron microscopy (SEM) images (Figure 1b; Figure S2, Supporting Information). The porous LMZP pellet prepared by CS at 1150 °C for 16 h shows relatively poor grain contact, while the LMZP pellet prepared by SPS shows good contact between particle grains. The powders sintered at 1150 °C by CS were used to prepare the dense SPS pellet. Therefore, LMZP prepared by SPS has a larger grain size than the sample prepared by CS, which also helps to reduce the grain boundary resistance. The improved contact between the grains of the SPS pellet could drastically reduce the  $\text{Li}^+$  grain boundary resistance.

The electrochemical impedance spectra of  $\text{Li}_{1+2x}\text{Mg}_x\text{Zr}_{2-x}(\text{PO}_4)_3$  pellets prepared by CS and SPS shown in Figure 1c and Figure S3 in the Supporting Information have two semicircles at the high and moderate frequencies, which correspond respectively to the  $\text{Li}^+$  movement in the bulk and across grain boundaries of  $\text{Li}_{1+2x}\text{Mg}_x\text{Zr}_{2-x}(\text{PO}_4)_3$ .  $\text{Li}_{1+2x}\text{Mg}_x\text{Zr}_{2-x}(\text{PO}_4)_3$  with  $x = 0.1$  ( $\text{Li}_{1.2}\text{Mg}_{0.1}\text{Zr}_{1.9}(\text{PO}_4)_3$ ; LMZP) has the highest bulk and total  $\text{Li}^+$  conductivities of  $1.2 \times 10^{-4}$  and  $2.8 \times 10^{-5}$  S cm<sup>-1</sup> at 25 °C, respectively. These conductivity values are much higher

than those of  $\text{LiZr}_2(\text{PO}_4)_3$  ( $10^{-6}$  S cm<sup>-1</sup> at 25 °C). The total  $\text{Li}^+$  conductivity of  $\text{Li}_{1.2}\text{Mg}_{0.1}\text{Zr}_{1.9}(\text{PO}_4)_3$  is further increased to  $4.2 \times 10^{-5}$  S cm<sup>-1</sup> at 25 °C with SPS (Figure 1c) by increasing the density of the pellet, which reduces grain boundary resistance. The cyclic voltammogram of a Li/LMZP/Au cell verified that the LMZP is stable up to 5.5 V versus  $\text{Li}^+/\text{Li}$  (Figure S3d, Supporting Information). The activation energies for  $\text{Li}^+$  transport of the  $\text{Li}_{1.2}\text{Mg}_{0.1}\text{Zr}_{1.9}(\text{PO}_4)_3$  sintered by CS and SPS are 0.40 and 0.36 eV (Figure 1d), respectively. Activation energies on this scale are similar to those of other solid electrolytes with fast  $\text{Li}^+$  conductivity, such as the garnet  $\text{Li}_7\text{La}_3\text{Zr}_2\text{O}_{12}$ .<sup>[29]</sup> Doping NASICON electrolytes can stabilize the fast Li-ion conducting rhombohedral phase. Further aliovalent doping for  $\text{P}^{5+}$  or  $\text{Zr}^{4+}$  ions in this material could provide an additional pathway to increase the concentration of mobile  $\text{Li}^+$ -ions, potentially improving its bulk Li-ion conductivity.

The chemical stability of  $\text{Li}_{1.2}\text{Mg}_{0.1}\text{Zr}_{1.9}(\text{PO}_4)_3$  in air was investigated with thermogravimetric analysis (TGA). The TGA results of LMZP pellets aged in air ( $\approx 15\%$  relative humidity) for 30 days (Figure S4a, Supporting Information) show no weight loss at temperatures from 25 to 600 °C, indicating that the material did not absorb any species from ambient atmosphere, such as  $\text{H}_2\text{O}$ . The fresh and aged LMZP samples had similar XRD results (Figure S4b, Supporting Information), confirming that LMZP is stable in air. The air-stability of LMZP, which can be related to the strong covalent bonding between  $\text{P}^{5+}\text{-O}^{2-}$  in the phosphate anion, could help increase the lithium metal wettability of the pellet by negating the formation of a  $\text{Li}^+$ -insulating surface layer such as  $\text{Li}_2\text{CO}_3$  and/or  $\text{LiOH}$ .

$^6\text{Li}$  solid-state NMR was employed to study the local  $\text{Li}^+$  environments and mobilities in  $\text{Li}_{1.2}\text{Mg}_{0.1}\text{Zr}_{1.9}(\text{PO}_4)_3$ . Figure 2 summarizes the high-resolution  $^7\text{Li}$  and  $^6\text{Li}$  MAS (25 kHz) NMR spectra, and  $^7\text{Li}$   $T_1$  relaxation time measurement of LMZP. Three individual peaks are necessary to simulate the whole  $^7\text{Li}$  lineshape in the spectrum of Figure 2a. Of these three peaks, two sharp resonances ( $-0.93$  ppm, blue;  $-0.67$  ppm, brown) are superimposed on a broad component at  $-0.9$  ppm (green dotted line). The two narrower peaks are ascribed to the  $+1/2 \leftrightarrow -1/2$  central transition, while the broad component underneath originates

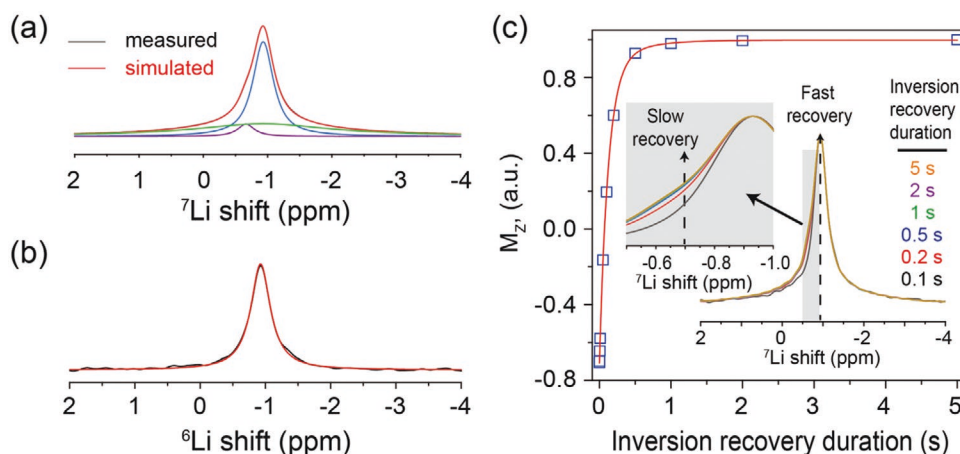


**Figure 2.** a)  $^7\text{Li}$  and b)  $^6\text{Li}$  MAS NMR spectra, and c)  $^7\text{Li}$  NMR spectra of  $\text{Li}_{1.2}\text{Mg}_{0.1}\text{Zr}_{1.9}(\text{PO}_4)_3$  extracted from  $^7\text{Li}$   $T_1$  relaxation time measurement. Central transitions are filled with colors for the sake of clarity. The blue and purple lines in (a) represent two Li-ion local environments, and the green line is originated from the satellite transition.

from satellite transitions ( $3/2 \leftrightarrow 1/2$  and  $-1/2 \leftrightarrow -2/3$ ).<sup>[30]</sup> This characteristic of  $^7\text{Li}$  NMR lineshape is commonly observed in polymer, glass-ceramic, and glass electrolytes as well as crystalline solid electrolytes.<sup>[31–33]</sup> Simulation of the LMZP  $^7\text{Li}$  spectrum results in a 9:1 integral ratio (blue peak:brown peak) when taking into account the contribution only from central transitions. This result confirms that most of the lithium resides in one crystallographic site in LMZP, which corroborates reported neutron powder diffraction data where 90% of  $\text{Li}^+$  sits in the sixfold disordered 36f tetrahedral site, and the remaining 10%  $\text{Li}^+$  ions occupy the threefold disordered 18e tetrahedral site.<sup>[30]</sup>

Simulation of the  $^6\text{Li}$  spectrum in Figure 2b shows one symmetric peak with a Lorentzian lineshape. The small missing component expected to appear at  $-0.67$  ppm, as in the  $^7\text{Li}$  spectrum, is likely attributed to the limited amount of Li sitting in the disordered 18e tetrahedral site as well as low sensitivity of  $^6\text{Li}$  NMR, rendering the  $-0.67$  ppm unresolved from the major resonance at  $-0.93$  ppm.<sup>[34]</sup> To rule out the possibility that the  $-0.67$  ppm resonance has a slow  $T_1$  relaxation resulting in its invisibility,  $^6\text{Li}$  spectra with varied recycle delays from 5 to 500 s were acquired (Figure S5, Supporting Information). The nearly identical lineshape in these  $^6\text{Li}$  spectra rules out this possibility. A relatively rapid relaxation of  $^6\text{Li}$  magnetization, which is induced by fast ion dynamics, is implied from the Lorentzian lineshape identified in the  $^6\text{Li}$  spectrum of LMZP; otherwise, a Gaussian-type lineshape due to orientation-dependent shifts should be observed in  $^6\text{Li}$  spectra with longer recycle delays.

We probed the Li-ion mobility in LMZP at room temperature with  $^7\text{Li}$   $T_1$  relaxation time measurements using an inversion-recovery approach. The recovery process of the magnetization is illustrated in the inset of Figure 2c. As the time duration after inversion increases, which shows that the  $-0.93$  ppm resonance recovers much faster than the  $-0.67$  ppm resonance. To more quantitatively analyze the difference, the recovery curve in Figure 2c shows the kinetics for the inverted magnetization returning to its equilibrium. This curve was fitted with a biexponential function, giving rise to two  $^7\text{Li}$   $T_1$  relaxation times with different fractions. 85% of  $^7\text{Li}$  spins of the  $-0.93$  ppm resonance have a short relaxation time of 0.12 s, whereas those of the 0.67 ppm resonance LMZP have a much longer  $T_1$  of up to 0.45 s. Different  $T_1$  relaxation times suggest the difference in Li-ion mobility. The  $T_1$  relaxation time (0.12 s) for the majority of the  $\text{Li}^+$ -ions is as short as the reported value for the garnet fast  $\text{Li}^+$ -ion conductor  $\text{Li}_7\text{La}_3\text{Zr}_2\text{O}_{12}$ , which implies the potential of LMZP to serve as a solid electrolyte for all-solid-state Li-ion batteries.

A symmetric Li/LMZP/Li cell was assembled to study the stability and  $\text{Li}^+$ -transfer at the Li/LMZP interface at  $60^\circ\text{C}$  and elucidate any interphase formation. The electrochemical impedance plot of the symmetric cell is shown in Figure 3a. The area-specific resistance of the Li/LMZP interface is about  $460\ \Omega\ \text{cm}^2$ , which is significantly lower than that of Li/untreated-garnet interface.<sup>[6]</sup> The Li/LMZP interfacial resistance rather than the bulk ionic resistance of the solid electrolyte dominates the total resistance of the cell. Cycling the symmetric Li/LMZP/Li cell at

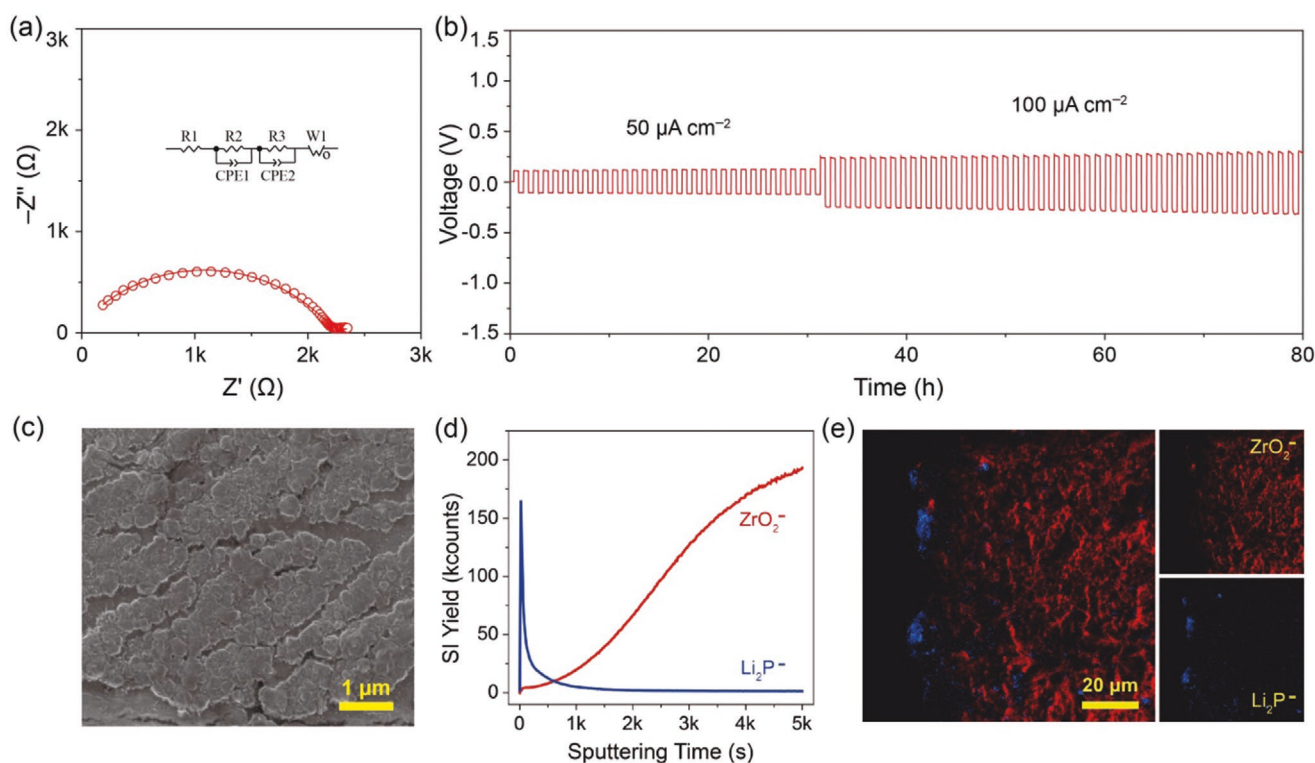


**Figure 3.** Symmetric Li/LMZP/Li cell at  $60^\circ\text{C}$ . a) Electrochemical impedance spectra with the fitting of the symmetric Li/LMZP/Li cell. b) Li/LMZP/Li symmetric cell cycling at different current densities at  $60^\circ\text{C}$ . Ex situ characterization of the LMZP pellet after symmetric Li/LMZP/Li cell cycling: c) SEM of lithium metal surface after cycling in a Li/LMZP/Li cell. d) TOF-SIMS depth profiles of  $\text{Li}_2\text{P}^-$  and  $\text{ZrO}_2^-$ , representing the  $\text{Li}_3\text{P}$  and LMZP, respectively. e) High-resolution cross-sectional chemical map of the LMZP pellet; the interfacial  $\text{Li}_3\text{P}$  layer is partially attached to the lithium foil during battery disassembly.



50 and 100  $\mu\text{A cm}^{-2}$  (Figure 3b) showed an overpotential of 0.12 and 0.25 V, respectively, with no clear additional overpotential increase within 80 h. This symmetric cell data with LMZP is promising as it does not require any other surface treatments or modifications to achieve stable cycling at room temperature. Other solid electrolyte materials, e.g., the garnet family, usually require a Li-alloy buffering layer or a polymer layer to avoid a short-circuit and stabilize the solid electrolyte/lithium metal interface. These modifications are even necessary at low current densities. SEM images of lithium metal cycled in a Li/LMZP/Li symmetric cell show no evidence of dendrite nucleation (Figure 3c), indicating uniform plating/stripping of the lithium-metal anode during cycling and good wettability of the LMZP electrolyte by the Li-metal anode.

The surface of the LMZP pellet changed color, becoming black, when contacted with lithium metal or was cycled in the symmetric Li/LMZP/Li cell. This color change indicates a chemical reaction between the Li metal and the LMZP electrolyte. TOF-SIMS depth profiling and high-resolution cross-sectional chemical mapping on the Li/LMZP interface were performed to elucidate the Li/LMZP interfacial reaction. From the observation of the obtained depth profiles, representative species were chosen to represent each component: 1) the interfacial layer, and 2) the bulk LMZP electrolyte.  $\text{Li}_2\text{P}^-$  was selected to represent the interfacial  $\text{Li}_3\text{P}$  layer that forms at the solid electrolyte/Li-metal interface while  $\text{ZrO}_2^-$  was selected to represent the bulk LMZP

electrolyte. The superimposed depth profiles of these species are shown in Figure 3d.  $\text{Li}_3\text{P}$  from the reaction between the metallic lithium anode and LMZP has a high concentration after low sputtering times, representing a high species concentration at the surface of the pellet that was in contact with lithium metal.<sup>[26,35]</sup> This result is confirmed with the high-resolution cross-sectional mapping of the Li/LMZP interface in Figure 3e, showing the surface of LMZP was covered by  $\text{Li}_3\text{P}$  with a thickness of about 3  $\mu\text{m}$ . Although the LMZP electrolyte is not itself stable against lithium metal, the in situ formed  $\text{Li}_3\text{P}$  layer has been shown to be a good  $\text{Li}^+$ -ion conductor. Thus, this in situ formed  $\text{Li}_3\text{P}$  layer that forms at the Li/LMZP interface 1) provides a high  $\text{Li}^+$  conductivity across the Li/LMZP interface, 2) maintains a good contact between the metallic lithium anode and LMZP during cycling, and 3) suppresses the lithium-dendrite nucleation and growth by homogenizing the current density on the plating/stripping Li-metal surface. Tailoring the composition of a solid electrolyte to introduce a self-limiting Li-ion conducting and electronically insulating passivation layer at the Li/electrolyte interface is a useful strategy to suppress lithium dendrite growth and achieve stable lithium plating/stripping.

Once the anode/electrolyte interface was clarified, the cathode interface and all-solid-state battery performance of the LMZP electrolyte was studied with a Li/LMZP/LiFePO<sub>4</sub> cell. The electrochemical impedance spectra of the cell is provided in Figure 4a. The cathode composite/electrolyte interfacial

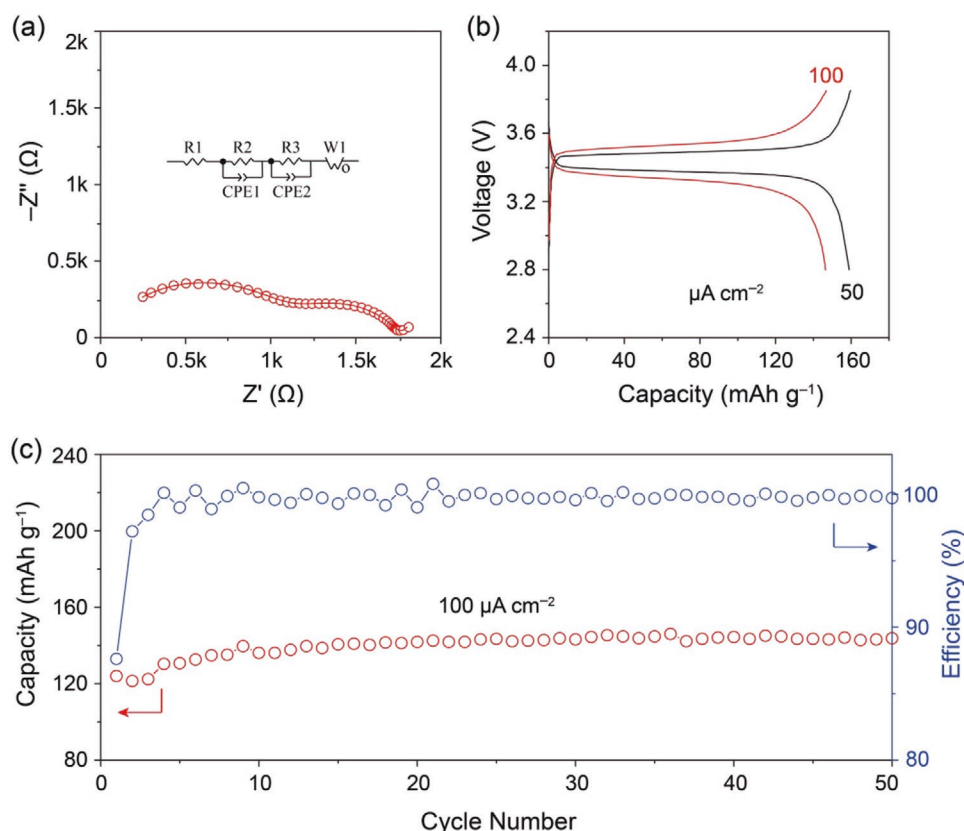


**Figure 4.** All-solid-state Li/LMZP/LiFePO<sub>4</sub> cell at 60 °C. a) The electrochemical impedance plots of the Li/LMZP/LiFePO<sub>4</sub> cell. b) Galvanostatic charge/discharge voltage profiles. c) Capacity retention and cycling efficiency of the Li/LMZP/LiFePO<sub>4</sub> cell. The active material loading of LiFePO<sub>4</sub> is 3–5  $\text{mg cm}^{-2}$ , and the thickness of the lithium foil is about 0.1 mm.

resistance is  $330 \Omega \text{ cm}^2$ , which is much lower than those found for the fast  $\text{Li}^+$  conducting garnet electrolyte.<sup>[36,37]</sup> Galvanostatic cycling of the Li/LMZP/LiFePO<sub>4</sub> cell at a current density of  $0.1 \text{ mA cm}^{-2}$  was performed in the voltage window of 3.85 to 2.8 V (Figure 4b); the cell has a discharge capacity of 155 and 140  $\text{mAh g}^{-1}$  at 0.05 and  $0.1 \text{ mA cm}^{-2}$ , respectively, with a high Coulombic efficiency of about 99.5%. This stable cycling shows the stability of the LMZP/LiFePO<sub>4</sub> interface. The cell showed 90% capacity retention after 50 charge/discharge cycles (Figure 4c).

### 3. Conclusion

The introduction of  $\text{Mg}^{2+}$  into  $\text{LiZr}_2(\text{PO}_4)_3$  stabilizes the fast-ion conducting rhombohedral NASICON-structure at room temperature and increases the  $\text{Li}^+$  concentration in the framework structure. Particularly, the rhombohedral  $\text{Li}_{1.2}\text{Mg}_{0.1}\text{Zr}_{1.9}(\text{PO}_4)_3$  phase showed two orders of magnitude higher  $\text{Li}^+$  conductivity than the triclinic  $\text{LiZr}_2(\text{PO}_4)_3$  phase at 25 °C. The strong  $\text{Li}^+$ – $\text{Li}^+$  Coulombic repulsion in the NASICON framework distributes the  $\text{Li}^+$  into two different crystallographic sites and reduces the activation energy for  $\text{Li}^+$  movement. The surface reduction of  $\text{Li}_{1.2}\text{Mg}_{0.1}\text{Zr}_{1.9}(\text{PO}_4)_3$  by a metallic Li-anode generates the in situ formation of an  $\text{Li}_3\text{P}$  interphase that improves the wettability of  $\text{Li}_{1.2}\text{Mg}_{0.1}\text{Zr}_{1.9}(\text{PO}_4)_3$  by the Li-metal anode and suppresses the nucleation and growth of lithium dendrites. Symmetric Li/LMZP/Li cells and an all-solid-state Li/LMZP/LiFePO<sub>4</sub> battery demonstrate the interfacial stability of the  $\text{Li}_{1.2}\text{Mg}_{0.1}\text{Zr}_{1.9}(\text{PO}_4)_3$  solid electrolyte at the anode/electrolyte interface and the cathode/electrolyte interface, respectively. The good cycling of these cells is enabled by the stability of the electrode/electrolyte interfaces that manifest small interfacial resistances, allowing for greater Coulombic efficiency and capacity retention.

### 4. Experimental Section

**Preparation of  $\text{Mg}^{2+}$ -Doped  $\text{LiZr}_2(\text{PO}_4)_3$ :**  $\text{Li}_{1+2x}\text{Mg}_x\text{Zr}_{2-x}(\text{PO}_4)_3$  ( $0.05 \leq x \leq 0.15$ ) materials were prepared with a traditional solid-state reaction. A stoichiometric amount of  $\text{LiNO}_3$ ,  $\text{Mg}(\text{NO}_3)_2$ ,  $\text{ZrO}_2$ , and  $(\text{NH}_4)_2\text{HPO}_4$  were ball-milled for 6 h with a 20 wt% excess of  $\text{LiNO}_3$  to compensate for  $\text{Li}_2\text{O}$  loss at elevated temperatures generated during milling. The powders were then sintered at 950 °C for 10 h to decompose the residual nitrates, and the obtained product was ball-milled again for 12 h. The  $\text{Li}_{1+2x}\text{Mg}_x\text{Zr}_{2-x}(\text{PO}_4)_3$  powders were then pressed into pellets and fired at 900–1150 °C for 16 h in a box furnace. The powders sintered at 1150 °C were used to prepare dense  $\text{Li}_{1.2}\text{Mg}_{0.1}\text{Zr}_{1.9}(\text{PO}_4)_3$  pellets via SPS at different temperatures (900–1150 °C) for 10 min with an applied pressure of 50 MPa.

**Material Characterization:** The phase composition of the  $\text{Li}_{1+2x}\text{Mg}_x\text{Zr}_{2-x}(\text{PO}_4)_3$  ( $0.05 \leq x \leq 0.15$ ) solid electrolytes was determined with powder X-ray diffraction. The fracture surface morphology of the pellets was observed with a field-emission scanning electron microscope. The composition of the  $\text{Li}_{1+2x}\text{Mg}_x\text{Zr}_{2-x}(\text{PO}_4)_3$  sample with  $x = 0.1$  was measured with the inductively coupled plasma-optical emission spectroscopy (ICP-OES). Electrochemical impedance spectroscopy was performed with a perturbation amplitude of 10 mV in the frequency range of 1 MHz to 1 Hz at varying temperatures between 298 and 370 K on an Autolab potentiostat to measure the A.C. impedance of these materials; Au was sputtered on both sides of the pellet to serve as  $\text{Li}^+$ -blocking electrode for this measurement. An Arrhenius model was used to fit the conductivity data and extract the

activation energy for the materials shown in Figure 1d. More than three pellets of each  $\text{Li}_{1+2x}\text{Mg}_x\text{Zr}_{2-x}(\text{PO}_4)_3$  composition were tested to confirm the  $\text{Li}^+$  conductivity; the error range of the resistance was less than 6%. Cyclic voltammetry (CV) was performed on an Auto-Lab workstation with a Li/LMZP/Au cell to check the electrochemical stability of LMZP.

$^6\text{Li}$  solid-state magic-angle spinning (MAS) NMR experiments were performed on a Bruker 500 spectrometer (11.75 T) equipped with a 2.5 mm HXY Bruker probe. MAS rate was set to 25 kHz, and the operating Larmor frequencies of  $^6\text{Li}$  and  $^7\text{Li}$  were 73.6 and 194.4 MHz, respectively.  $^6\text{Li}$  NMR spectra were collected using a single-pulse sequence with a solid  $90^\circ$  pulse length of 4.75  $\mu\text{s}$  with a variety of recycle delay from 5 to 500 s.  $^7\text{Li}$  NMR spectra were collected using a rotor-synchronized spin-echo pulse sequence. A solid  $90^\circ$  pulse length of 3.35  $\mu\text{s}$  and a recycle delay of 2 s was used. The  $^6\text{Li}$  NMR shift was referenced to  $\text{LiCl}_3$  at  $-1.1$  ppm. Rotor-synchronized (MAS = 25 kHz) spin-echo pulse sequence and single-pulse sequence were employed to acquire  $^7\text{Li}$  spectra with a  $90^\circ$  pulse length of 3.35  $\mu\text{s}$  (R.F. field  $\approx 74$  kHz) and a recycle delay of 2 s.  $^6\text{Li}$  spectra were obtained via a single pulse with a solid  $90^\circ$  pulse length of 4.75  $\mu\text{s}$  (R.F. field  $\approx 52$  kHz) and varied recycle delay from 5 to 500 s.  $^7\text{Li}$   $T_1$  relaxation time was measured using an inversion-recovery sequence.  $^6\text{Li}$  chemical shift was referenced to  $\text{LiCl}_3$  at  $-1.1$  ppm.

An LMZP pellet of 350  $\mu\text{m}$  thickness and a metallic lithium anode with a surface area of 0.5  $\text{cm}^2$  were used in all battery testing, symmetric cells, and full cells. The symmetric Li/LMZP/Li cell was cycled at 60 °C at different current densities. The area-specific resistance (ASR) was calculated with the equation:  $R_{\text{ASR}} = ((R_{\text{Total}} - R_{\text{LMZP}})/2) \times S$ ;  $R_{\text{Total}}$ ,  $R_{\text{LMZP}}$ , and  $S$  are the total resistance of the symmetric cell, the resistance of the pellet, and the Li/LMZP contact surface area (0.5  $\text{cm}^2$ ), respectively. The symmetric cell after cycling was disassembled in the glovebox for the SEM characterization and ex situ TOF-SIMS characterization. The TOF-SIMS analysis was performed on a ION-TOF GmbH (2010) TOF. SIMS 5 instrument equipped with a  $\text{Bi}^+$  analysis ion gun and a dual sputtering ( $\text{Cs}^+$  and  $\text{O}_2^+$ ) ion gun. The depth profiles were acquired with the analysis ion gun setup in high current (H.C.) mode ( $\text{Bi}^+$  at 30 keV ion energy,  $\approx 3.7$  pA measured sample current) and raster scanned over  $100 \times 100 \mu\text{m}^2$  areas, while the sputtering gun, using the  $\text{Cs}^+$  source (2 keV ion energy and  $\approx 70$  nA measured sample current), was raster scanned over  $300 \times 300 \mu\text{m}^2$  areas, centered around the analyzed areas.

An all-solid-state Li/LMZP/LiFePO<sub>4</sub> cell was assembled with a Li anode, a LMZP pellet as the solid electrolyte, and a LiFePO<sub>4</sub> composite cathode. The LiFePO<sub>4</sub> cathode was prepared by mixing LiFePO<sub>4</sub>, carbon black, polyethylene oxide, and LiTFSI with a weight ratio of 60:12:20:8. Ten cells were assembled and tested to verify the cycling performance of the Li/LMZP/LiFePO<sub>4</sub> all-solid-state batteries; these cells were cycled between 2.8 and 3.85 V versus  $\text{Li}^+/\text{Li}$  with a LAND battery tester.

### Supporting Information

Supporting Information is available from the Wiley Online Library or from the author.

### Acknowledgements

Q.Y.Z. and B.Y.X. contributed equally to this work. This work was primarily supported by the U.S. Department of Energy, Office of Basic Energy Sciences, Division of Materials Science and Engineering under award number DE-SC0005397. J.B.G. would like to acknowledge the support of the Robert A. Welch Foundation, Houston, Texas (Grant No. F-1066). The NMR experiment was supported by the National Science Foundation under Grant No. DMR-1808517. All-solid-state NMR experiments were performed at the National High Magnetic Field Laboratory. The National High Magnetic Field Laboratory is supported by the National Science Foundation through NSF/DMR-1644779 and the State of Florida. Q.Y.Z. thanks his university for the funding support to work at the University of Texas at Austin.

## Conflict of Interest

The authors declare no conflict of interest.

## Keywords

all-solid-state Li-metal batteries, interfacial stability, Li-ion environments, lithium dendrites, NASICON electrolytes

Received: August 24, 2020

Published online:

- [1] Q. Zhao, S. Stalin, C.-Z. Zhao, L. A. Archer, *Nat. Rev. Mater.* **2020**, 5, 229.
- [2] T. Nakamura, K. Amezawa, J. Kulisch, W. G. Zeier, J. Janek, *ACS Appl. Mater. Interfaces* **2019**, 11, 19968.
- [3] A. Manthiram, X. Yu, S. Wang, *Nat. Rev. Mater.* **2017**, 2, 16103.
- [4] M. Weiss, F. J. Simon, M. R. Busche, T. Nakamura, D. Schröder, F. H. Richter, J. Janek, *Electrochem. Energy Rev.* **2020**, 3, 221.
- [5] J. Janek, W. G. Zeier, *Nat. Energy* **2016**, 1, 16141.
- [6] Y. Li, B. Xu, H. Xu, H. Duan, X. Lu, S. Xin, W. Zhou, L. Xue, G. Fu, A. Manthiram, J. B. Goodenough, *Angew. Chem., Int. Ed. Engl.* **2017**, 56, 753.
- [7] J. Liang, Q. Sun, Y. Zhao, Y. Sun, C. Wang, W. Li, M. Li, D. Wang, X. Li, Y. Liu, K. Adair, R. Li, L. Zhang, R. Yang, S. Lu, H. Huang, X. Sun, *J. Mater. Chem. A* **2018**, 6, 23712.
- [8] H. Zhou, Y. Wang, H. Li, P. He, *ChemSusChem* **2010**, 3, 1009.
- [9] N. Kamaya, K. Homma, Y. Yamakawa, M. Hirayama, R. Kanno, M. Yonemura, T. Kamiyama, Y. Kato, S. Hama, K. Kawamoto, A. Mitsui, *Nat. Mater.* **2011**, 10, 682.
- [10] A. Kuhn, O. Gerbig, C. Zhu, F. Falkenberg, J. Maier, B. V. Lotsch, *Phys. Chem. Chem. Phys.* **2014**, 16, 14669.
- [11] Y. Li, C.-A. Wang, H. Xie, J. Cheng, J. B. Goodenough, *Electrochem. Commun.* **2011**, 13, 1289.
- [12] B. Lang, B. Ziebarth, C. Elsässer, *Chem. Mater.* **2015**, 27, 5040.
- [13] P. Zhang, M. Matsui, A. Hirano, Y. Takeda, O. Yamamoto, N. Imanishi, *Solid State Ionics* **2013**, 253, 175.
- [14] M. Kotobuki, M. Koishi, Y. Kato, *Ionics* **2013**, 19, 1945.
- [15] F. Ma, E. Zhao, S. Zhu, W. Yan, D. Sun, Y. Jin, C. Nan, *Solid State Ionics* **2016**, 295, 7.
- [16] V. Thangadurai, W. Weppner, *Ionics* **2000**, 6, 70.
- [17] Y. Li, W. Zhou, S. Xin, S. Li, J. Zhu, X. Lu, Z. Cui, Q. Jia, J. Zhou, Y. Zhao, J. B. Goodenough, *Angew. Chem., Int. Ed. Engl.* **2016**, 55, 9965.
- [18] L. Cheng, E. Crumlin, W. Chen, R. Qiao, H. Hou, S. Lux, V. Zorba, R. Russo, R. Kostecki, Z. Liu, K. Persson, W. Yang, J. Cabana, T. Richardson, G. Chen, M. Doeff, *Phys. Chem. Chem. Phys.* **2014**, 16, 18294.
- [19] W. Xia, B. Xu, H. Duan, Y. Guo, H. Kang, H. Li, H. Liu, *ACS Appl. Mater. Interfaces* **2016**, 8, 5335.
- [20] P. Hartmann, T. Leichtweiss, M. R. Busche, M. Schneider, M. Reich, J. Sann, P. Adelhelm, J. Janek, *J. Phys. Chem. C* **2013**, 117, 21064.
- [21] Y. Liu, Q. Sun, Y. Zhao, B. Wang, P. Kaghazchi, K. R. Adair, R. Li, C. Zhang, J. Liu, L. Y. Kuo, Y. Hu, T. K. Sham, L. Zhang, R. Yang, S. Lu, X. Song, X. Sun, *ACS Appl. Mater. Interfaces* **2018**, 10, 31240.
- [22] B. Wu, S. Wang, J. Lochala, D. Desrochers, B. Liu, W. Zhang, J. Yang, J. Xiao, *Energy Environ. Sci.* **2018**, 11, 1803.
- [23] Y. Zhu, X. He, Y. Mo, *J. Mater. Chem. A* **2016**, 4, 3253.
- [24] K. Arbi, M. A. Paris, J. Sanz, *J. Phys. Chem. B* **2006**, 110, 6454.
- [25] H. Xie, J. B. Goodenough, Y. Li, *J. Power Sources* **2011**, 196, 7760.
- [26] Y. Li, W. Zhou, X. Chen, X. Lu, Z. Cui, S. Xin, L. Xue, Q. Jia, J. B. Goodenough, *Proc. Natl. Acad. Sci. USA* **2016**, 113, 13313.
- [27] Y. Li, M. Liu, K. Liu, C.-A. Wang, *J. Power Sources* **2013**, 240, 50.
- [28] M. Catti, A. Comotti, S. Di Blas, *Chem. Mater.* **2003**, 15, 1628.
- [29] Z. Zhang, Y. Shao, B. Lotsch, Y.-S. Hu, H. Li, J. Janek, L. F. Nazar, C.-W. Nan, J. Maier, M. Armand, L. Chen, *Energy Environ. Sci.* **2018**, 11, 1945.
- [30] M. C. Paulus, M. F. Graf, P. Harks, A. Paulus, P. P. M. Schleker, P. H. L. Notten, R. A. Eichel, J. Granwehr, *J. Magn. Reson.* **2018**, 294, 133.
- [31] K. Hayamizu, Y. Terada, K. Kataoka, J. Akimoto, *J. Chem. Phys.* **2019**, 150, 194502.
- [32] P. Heitjans, M. Wilkening, *MRS Bull.* **2009**, 34, 915.
- [33] Y. Xiang, X. Li, Y. Cheng, X. Sun, Y. Yang, *Mater. Today* **2020**, 36, 139.
- [34] Z. Jian, Y. S. Hu, X. Ji, W. Chen, *Adv. Mater.* **2017**, 29, 1601925.
- [35] H. El-Shinawi, A. Regoutz, D. J. Payne, E. J. Cussen, S. A. Corr, *J. Mater. Chem. A* **2018**, 6, 5296.
- [36] X. Han, Y. Gong, K. K. Fu, X. He, G. T. Hitz, J. Dai, A. Pearce, B. Liu, H. Wang, G. Rubloff, Y. Mo, V. Thangadurai, E. D. Wachsman, L. Hu, *Nat. Mater.* **2017**, 16, 572.
- [37] K. Fu, Y. Gong, B. Liu, Y. Zhu, S. Xu, Y. Yao, W. Luo, C. Wang, S. D. Lacey, J. Dai, Y. Chen, Y. Mo, E. Wachsman, L. Hu, *Sci. Adv.* **2017**, 3, e1601659.